Journal of Alloys and Compounds 976 (2024) 173196

Contents lists available at ScienceDirect

Journal of Alloys and Compounds

journal homepage: www.elsevier.com/locate/jalcom

Microstructure stability and self-diffusion in the equiatomic HfScTiZr HCP multi-principal element alloy

G. Mohan Muralikrishna [a,*], Sandipan Sen [a], Sai Kumaran Ayyappan [b], S. Sankaran [b], K. Guruvidyathri [c], Juliana Schell [d,e], Lukasz Rogal [f], Xi Zhang [g], Joachim Mayer [h,i], Blazej Grabowski [g], Gerhard Wilde [a], Sergiy V. Divinski [a,*]

[a] Institute of Materials Physics, University of Münster, Wilhelm-Klemm-Str. 10, 48149 Münster, Germany
[b] Department of Metallurgical and Materials Engineering, Indian Institute of Technology, Madras 600036, Chennai, India
[c] School of Engineering Sciences and Technology, University of Hyderabad, Prof CR Rao Road, Gachibowli, Hyderabad 500046, India
[d] European Organization for Nuclear Research (CERN), CH-1211 Geneva, Switzerland
[e] Institute for Materials Science and Center for Nanointegration Duisburg-Essen (CENIDE), University of Duisburg-Essen, Essen, Germany
[f] Institute of Metallurgy and Materials Science, Polish Academy of Sciences, Reymonta 25 St., 30-059, Krakow, Poland
[g] Institute for Materials Science, University of Stuttgart, Pfaffenwaldring 55, Stuttgart 70569, Germany
[h] Central Facility for Electron Microscopy, RWTH Aachen University, 52074 Aachen, Germany
[i] Ernst Ruska-Centre for Microscopy and Spectroscopy with Electrons, Forschungszentrum Jülich, 52425 Jülich, Germany

ARTICLE INFO

Keywords:
High-Entropy alloy
Tracer Diffusion
Phase transformation
Phase stability
Density Functional Theory
Phase Diagrams
CALPHAD

ABSTRACT

Tracer diffusion of ^{44}Ti, ^{46}Sc and ^{89}Zr in the hexagonal close-packed (HCP) HfScTiZr multicomponent alloy is investigated using the radiotracer technique. The microstructure stability is thoroughly examined by conducting prolonged heat treatments between 873 K and 1373 K to mimic the diffusion conditions. Electron microscopy analysis reveals that the alloy contains a mixture of two HCP phases with similar lattice constants, among which the major phase is enriched in Sc, whereas the minor phase is strongly enriched in Ti. The thermal stability is assessed by *ab initio*-informed calculations which support the existence of the two HCP phases. The Sc diffusion coefficients differ markedly between the HCP phases, while only marginal influence is found for the diffusion of Zr and Ti. The Arrhenius parameters are determined, i.e., the activation energy and the pre-factor. The diffusion properties are analyzed in correlation with the microstructure stability and the *ab initio*-informed thermodynamic results. The DFT-calculated mean squared atomic displacements, which represent the lattice distortions, are found to provide an appropriate parameter for predicting the diffusion trends of the individual elements. The phase analysis is further compared with existing CALPHAD-type predictions, and the discrepancies between the theoretical assessments and experimental observations are examined and discussed.

1. Introduction

The material design concept based on multi-principal-element alloys has opened a wide range of opportunities for fundamental research and technological applications [1]. These chemically complex single-phase materials are known as high-entropy alloys (HEAs) [2,3]. Many of these alloys form simple solid solutions at elevated temperatures, mainly featuring the face-centered cubic (FCC) or body-centered cubic (BCC) lattices. With a careful selection of constituent elements and alloy compositions, eutectic mixtures [4] or ordered compounds [5] of particular relevance to high-temperature applications can be fabricated [6]. HEAs were reported to exhibit several beneficial properties such as high fatigue resistance [7], excellent thermal stability [8–10], resistance to irradiation [11], excellent oxidation resistance [12], high hardness [13], wear resistance [14], good corrosion resistance [15], and high-temperature strength [16]. Since these extraordinary properties are often achieved or controlled via various diffusion-related phenomena, an exact determination of the corresponding diffusion rates is paramount for fundamental understanding and for the ability to engineer the properties of high-entropy alloys.

Among the four core effects of HEAs, "sluggish" (retarded) diffusion was proposed to be the fundamental reason for the excellent phase

* Corresponding authors.
E-mail addresses: garlapat@uni-muenster.de, mohanmuralikrishna9@gmail.com (G.M. Muralikrishna), divin@uni-muenster.de (S.V. Divinski).

https://doi.org/10.1016/j.jallcom.2023.173196
Received 6 October 2023; Received in revised form 13 December 2023; Accepted 14 December 2023
Available online 19 December 2023

stability and the retention of the mechanical properties at high temperatures [17]. Various studies dedicated to the investigation of diffusion in FCC (CoCrFeNi, CoCrFeMnNi) [18,19], BCC (HfTiZrNbV, HfTiZrNbTa) [20], or hexagonal close-packed (HCP) [21,22] multi-component and multi-principal-element alloys have been reported in recent years. Though most of those studies were devoted to FCC systems, see e.g., the recent reviews [23–25]. In some cases, these studies were extended to more complex single-phase alloys crystallizing as a B2 ordered structure [26,27], as a σ phase [28] or even as phase mixtures [29]. Eventually, the "sluggish" diffusion concept was demystified and relativized across various compositions and crystal lattices [23–25].

Nevertheless, research on diffusion in HCP multi-principal-element alloys remains quite scarce and to the best of our knowledge, is limited to only two reports [21,22]. This is mainly due to the exotic nature of the elements used to fabricate HCP HEAs [30,31] and the practical difficulties involved in the synthesis of these alloys [32]. Most of these HCP HEAs comprise rare-earth metals like Y, Gd, Tb, Dy, Ho, and Lu. Recently, a comprehensive investigation into the formation of HCP phases using *ab initio*-informed thermodynamic calculations was conducted for the Al–Hf–Sc–Ti–Zr system with the usage of only one rare earth element (Sc) [33]. *Ab initio* calculations of vacancy energetics in this system revealed an increase of vacancy concentration from regular binary to HEA systems [34]. These findings were directly validated through experimental measurements of Ti diffusion within these HCP HEAs [21].

Among the subsystems of the Al–Hf–Sc–Ti–Zr system, the HfScTiZr equiatomic alloy was found to exhibit a nearly single-phase HCP crystal structure [35] with a presence of less than 6 % of a second HCP phase. This equiatomic HfScTiZr HCP HEA was reported to exhibit a high strain hardening rate, leading to impressive yield and compressive strengths. Additionally, it is characterized by a very low electrical conductivity, making this alloy suitable for designing strain gauges or transducers [36]. However, a detailed exploration of the phase stability and diffusion behavior is noticeably absent, which is crucial for maintaining the above-mentioned properties.

In this study, we extensively examined the self-diffusion and thermal stability properties of the HfScTiZr HCP alloy. The self-diffusivities of Ti, Sc, and Zr are systematically measured using the radiotracer diffusion technique and the ^{44}Ti, ^{46}Sc, and ^{89}Zr radioisotopes. The elemental diffusivities are discussed in connection with the microstructure stability and corresponding physical properties of the alloying elements. These data are compared with the existing literature on related HCP HEAs and are analyzed in the context of the originally proposed [2] "sluggish diffusion concept" for high-entropy alloys. The experimental results of the thermal stability are evaluated using the calculation of phase diagrams (CALPHAD) method and density–functional–theory (DFT)–based Gibbs energy calculations.

2. Materials and methods

2.1. Alloy preparation and characterization

High-purity (99.99 %) raw materials of Hf, Sc, Ti, and Zr were mixed in equiatomic composition and melted in an arc melting furnace under a high-purity Ar atmosphere. The ingot was flipped after each melting and re-melted. This procedure was repeated at least five times to enable a uniform mixing of the alloying elements. Subsequently, the ingots were homogenized at 1423 K for 5 days. To maintain uniformity of the experimental procedure and to enable a correlation of the phase distribution and the diffusion behavior (conducted at 873–1373 K), the thermal stability of the observed phases was investigated at the highest (1373 K) and the lowest temperatures (873 K).

The homogenized samples were cut into cylindrical disks of 1 mm thickness and 10 mm diameter. The cut discs were pre-annealed at the intended diffusion annealing temperatures to release the stresses developed during the sample cutting. These pre-annealed samples were then metallographically polished to produce a mirror-like surface finish. The polished samples were used for the microstructure characterization and the tracer diffusion measurements.

X-ray diffraction was performed on the homogenized and heat-treated samples using a Philips PW 1410 Diffractometer using Cu-K_α ($\lambda = 1.5406\mathring{A}$) radiation and a diffractometer with $\theta - \theta$ geometry. The X-ray diffractograms were collected at a scanning rate of 0.02°/sec and a dwell time of 20 s for each step.

Characterization of the microstructure and the composition analysis of the homogenized and heat-treated samples were performed using a scanning electron microscope (SEM, FEI Nova NanoSEM 230) equipped with electron back-scatter diffraction (EBSD) and energy dispersive spectroscopy (EDS). The EBSD patterns were captured by focusing the electron beam onto the sample surface at a 70° tilted angle and a working distance of 15 mm. The obtained EBSD patterns were analyzed using the TSL-OIM software.

Transmission electron microscopy (TEM) specimens were prepared from the polished specimen by focused ion beam (FIB) milling using a Zeiss Crossbeam 350 system with Ga ions operating at 30 kV and the final thinning was performed with 5 kV.

TEM and electron diffraction measurements were performed by a FEI Tecnai F20 TEM at 200 kV. Analytical TEM measurements were performed with a Titan Themis G3 60–300 TEM operated at 300 kV and equipped with FEI's ChemiSTEM technology. Atomic scale HRSTEM imaging was performed with the TFS Spectra 300 microscope equipped with an XFEG probe and image Cs corrector and a super-X EDXS system operating at 300 kV. The convergence semi-angle for STEM imaging and EDXS chemical mapping was approximately 25 mrad, while the collection semi-angles were 80–220 mrad for HAADF imaging. EDXS maps were collected typically for around 45 min, and background subtraction was performed.

CALPHAD (calculation of phase diagrams) calculations were performed using the Thermo-Calc software™ along with the TCAL7 database.

2.2. Tracer diffusion measurements

The ^{89}Zr radioisotope (half-life of 3.3 days) was purchased from PerkinElmer LAS GmbH (Germany) in the form of an oxalic acid solution. The original solution was heavily diluted with double distilled water before being used for the tracer diffusion measurements.

The ^{44}Ti radioisotope (half-life of 60 years) was originally produced by exposing tiny rectangular Sc foils to proton irradiation. The details of the radio-chemical separation of Ti and Sc are given in Ref. [37]. The heavily irradiated foils were dissolved in an HCl solution. The ^{44}Ti isotope and the residual Sc were chemically separated using an anion exchange absorption in a concentrated HCl solution and further neutralized by dissolving NaOH capsules to obtain a pH-neutral solution. This solution was further diluted with double distilled water before being used for the diffusion experiments. A few microliters of the tracer solution with a specific activity of about 15–20 kBq (^{89}Zr) or 1–3 kBq (^{44}Ti) was deposited on the sample's surfaces and dried under a sodium vapor lamp.

The ^{46}Sc radioisotope was implanted using the high-energy Isotope mass Separator On-Line facility (ISOLDE) [38,39] at the European Organization for Nuclear Research (CERN) in Geneva, Switzerland. The ^{46}Sc beam was produced by irradiation of a ^{46}Ta target with a 1.4 GeV proton beam and simultaneous activation by a high-energy laser beam. The implanted samples were delivered to the radiotracer laboratory in Münster and subjected to diffusion annealing treatments.

The samples with deposited (Ti, Zr) or implanted (Sc) tracers were each wrapped in a Ta foil and sealed in an evacuated (5×10^{-5} mbar) quartz tube filled with high-purity Ar (99.999 %). The sealed quartz tubes were diffusion-annealed in a tubular furnace. The furnace temperature was measured using a calibrated Ni/NiCr (type K) external thermo-couple and controlled within ± 1 K. The diffusion-annealed

samples were reduced in diameter by 1 mm to eliminate a possible lateral or surface diffusion contribution. The samples were sectioned using a precision parallel sectioning device by mechanical grinding. The thickness of each section was determined by measuring the weight of the sample before and after each sectioning step using a micro-balance with an accuracy of ± 0.1 μg.

The relative specific activity of each section was measured by a solid NaI γ-detector equipped with a 16k multi-channel energy discriminator to count the γ-decays of ^{89}Zr, ^{44}Ti and ^{46}Sc. The counting times were adjusted to attain statistical uncertainty of better than 2 %. Using the multi-channel energy discriminator allowed for the reliable determination of the concentration profiles without any influence from background radiation. The experimental uncertainties of the relative specific activity in each section on the profiles, resulting from the sectioning, measuring the weight (depth determination) and from counting the radioactivity, were estimated to be typically less than 10 %. The penetration profiles were further processed to obtain the diffusion coefficients of the individual elements.

2.3. Ab initio calculations

To evaluate the temperature-dependent phase stability of the HfScTiZr alloy from theory, the Gibbs energy difference between the two-phase mixture and the single-phase HCP solid solution was computed by using a density-functional-theory (DFT) based supercell approach.[1] The Gibbs energy of each phase was described by the sum of the 0 K total energy and the contribution from configurational entropy, which means that contributions from other thermal excitations were ignored. For the related Al-Hf-Sc-Ti-Zr system, the configurational entropy was shown to be most critical for the phase stability prediction [33]. Note that the thermal excitations beyond the configurational entropy are still likely to modify the transition temperature as discussed in Section 4.1. For each phase with the experimental compositions given in Table 1, the 0 K total energy was obtained from full DFT ionic relaxations of one special quasi-random structure (SQS) of 96 atoms (4 × 4 × 3 expansion of the HCP primitive cell) as complete randomness without short-range order was assumed.

The configurational entropy was estimated based on the ideal mixing, i.e., $\Delta S_{\text{conf}} = -k_B \sum_{i=1}^{n} X_i \ln(X_i)$, where X_i is the atomic fraction of the element i in the phase and k_B is the Boltzmann constant.

The resulting Gibbs energy difference is expressed as:

$$\Delta G = f G_{\text{HCP}_1} + (1-f) G_{\text{HCP}_2} - G_{\text{HCP}} \quad (1)$$

Table 1
Composition of elements (in at %) in the bright (major) and dark (minor) phases in the HfScTiZr alloy determined by EDS (labeled "Experiment") and as predicted by CALPHAD calculations. The estimated experimental uncertainties are less than ± 0.5 at %.

Element	Major phase		Minor phase	
	Experiment	CALPHAD	Experiment	CALPHAD
Hf	26.8	24.56	20.8	26.52
Sc	28.5	41.61	12.8	5.82
Ti	20.2	6.29	45.1	47.74
Zr	24.4	27.54	21.3	19.93

[1] All DFT calculations in this work were performed employing the projector augmented wave (PAW) method [40] within the generalized gradient approximation (GGA) in the Perdew-Burke-Ernzerhof (PBE) parametrization [41], as implemented in VASP (version 5.4) [42,43]. The technical details, e.g., the employed PAW potentials, the plane wave cutoff, the number of k-points, and the convergence criteria, are the same as in Refs. [34,44].

where the subscripts HCP_1 and HCP_2 denote the Sc-rich and Ti-rich phases with the phase fractions of f and $1-f$, respectively, and HCP indicates the single-phase HCP solid solution.

To understand the influence of lattice distortions on the measured diffusivities in the HfScTiZr alloy, the mean squared atomic displacements (MSADs) were evaluated using DFT calculations. The ionic relaxations were performed using DFT calculations using a special quasi-random (SQS) structure built with 96 atoms for each alloy composition in the fully relaxed (volume and shape of the cell) condition, i.e., under the absence of pressure. The MSAD values were obtained using:

$$\text{MSAD} = \frac{1}{N}\sum_{i}^{N} \| \rightarrow r_i - \rightarrow r_{i,0} \|^2, \quad (2)$$

where $\rightarrow r_i$ and $\rightarrow r_{i,0}$ are the relaxed and ideal atomic coordinates of the atom i of the respective alloying element, and N is the number of atoms of the alloying element in the alloy.

3. Results

3.1. Phase stability of the HfScTiZr alloy

The crystal structure of the homogenized HfScTiZr multi-principal element alloy as characterized by X-ray diffraction is shown in Fig. 1 (a). Crystallographic reflections of a single HCP structure are found in the X-ray diffractogram. In contrast, the microstructure characterization by SEM reveals the presence of two distinct phases; see the back scattered electron (BSE) image in Fig. 1(b). The EDS analysis confirms different compositions of the major and minor phases, the lower panel of Fig. 1(b). Upon closer examination, the magnified view reveals that the second phase (minor phase) is distributed as a lamellar network. This phase is rich in Ti, significantly depleted in Sc, and slightly deficient in Hf and Zr, Table 1. The volume fraction of the minor phase is estimated to be about (20 ± 5) %.

The EBSD analysis, Fig. 1(c), reveals a large fraction of high-angle grain boundaries and a random texture. Similar to the XRD results, the EBSD phase map supports the presence of a single HCP phase. Taken together, the XRD and SEM+EBSD results thus suggest a mixture of two HCP phases with similar lattice constants that are difficult to distinguish with XRD.

A phase fraction plot for the HfScTiZr equiatomic alloy as obtained by CALPHAD calculations is shown in Fig. 2. The temperature window of the diffusion annealing experiments is highlighted. Experimentally, two HCP phases are observed upon annealing within the indicated temperature range. On the contrary, the CALPHAD-type calculations predict a phase decomposition to two HCP phases only below 1128 K.

Generally, when conducting diffusion measurements, it is crucial to ensure the stability of the material's microstructure during diffusion annealing treatment (otherwise, its evolution during diffusion annealing has to be carefully evaluated, and proper solutions have to be used [45]). To replicate the tracer diffusion experiments, phase stability studies were carried out at temperatures slightly above (at 1373 K) and somewhat below (at 873 K) the temperature range of the diffusion measurements.

The homogenized samples were additionally heat treated for 6 days at 1373 K and 11 days at 873 K. The HCP phases described earlier remain extremely stable even after prolonged heat treatments. Fig. 3(a) presents the X-ray diffractograms substantiating the presence of an HCP phase in the samples. While standard X-ray diffractograms do not resolve the presence of a second HCP phase, a meticulous analysis of the XRD patterns through a slow scan (presented as an inset in Fig. 3(a)) does indeed unveil the existence of two HCP phases. The microstructures of the samples subjected to the heat treatments at 1373 K and at 873 K are depicted in Fig. 3(b1) and (b2), respectively. The phase distribution is similar to the homogenized samples without any observable changes. Notably, the minor phase exhibits exceptional stability and is distributed

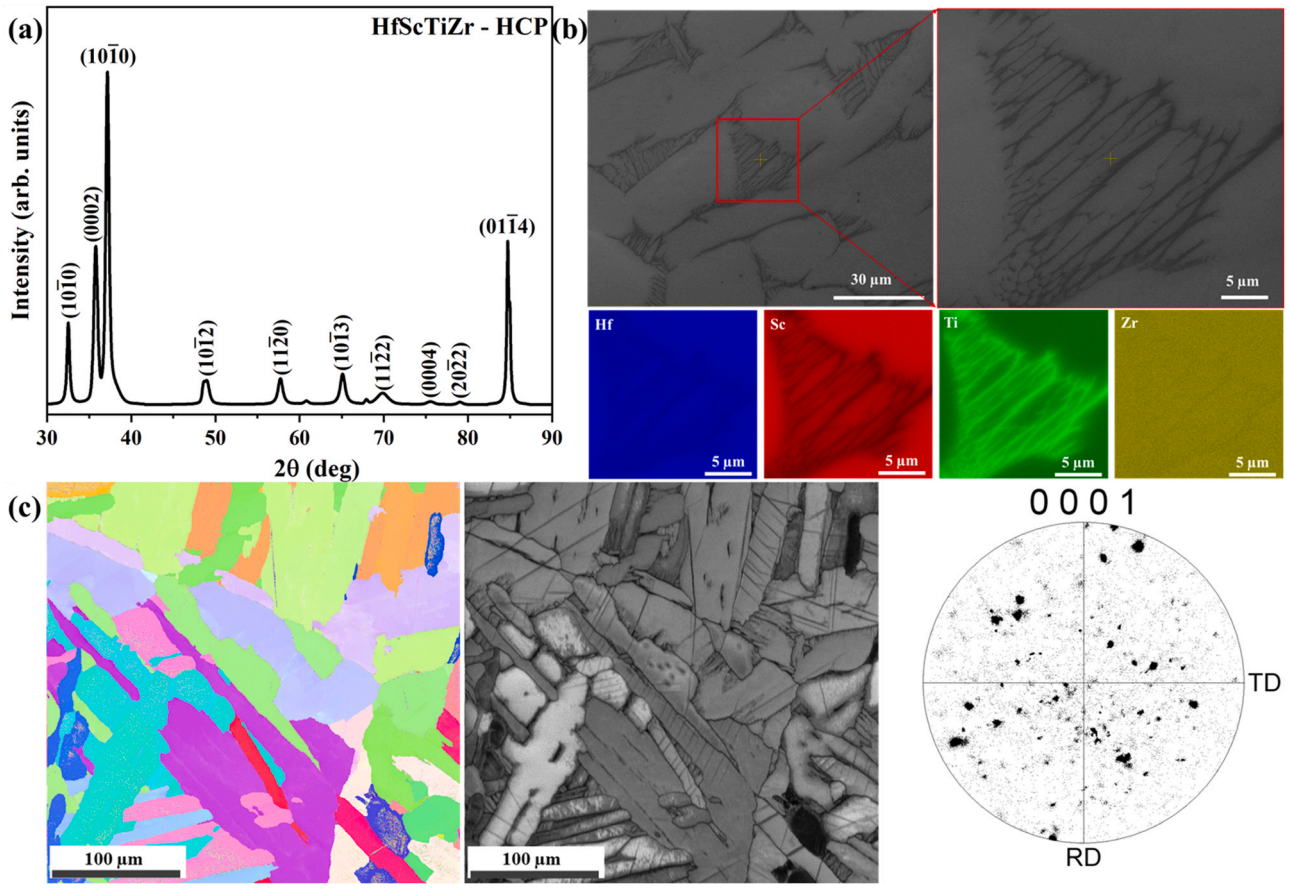

Fig. 1. Microstructure characterization of the HfScTiZr alloy in the homogenized condition: (a) XRD pattern with indexed HCP reflections; (b) Back scattered electron (BSE) image and corresponding elemental maps revealing the presence of two distinct phases; (c) Electron back scattered electron diffraction (EBSD) orientation map revealing predominantly high-angle grain boundaries and a nearly random texture, see (0001) pole figure, right panel. In (c), the presence of the two distinct HCP phases is not resolved by the EBSD mapping during the indexing of the Kikuchi patterns.

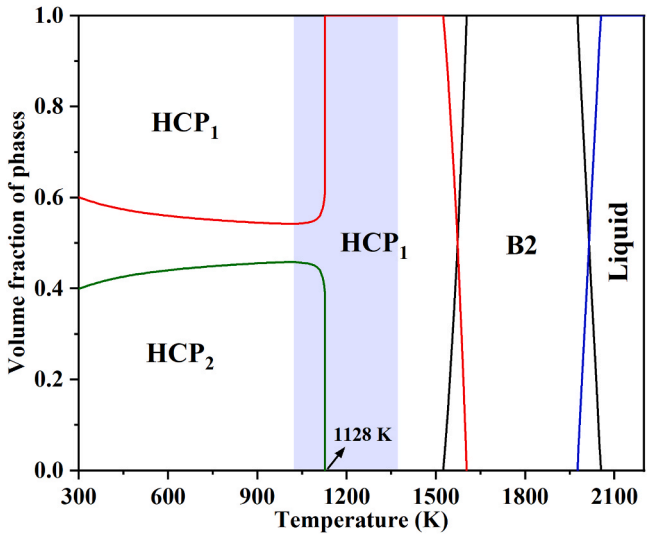

Fig. 2. Phase fraction plot for the HfScTiZr alloy as predicted by CALPHAD calculations. The shaded area indicates the temperature interval of the present measurements, which reveal a mixture of two HCP phases under the present experimental conditions.

as a lamellar network.

Fig. 3(c) presents a TEM bright field image of the heat-treated HfScTiZr alloy. The crystallographic characteristics of both major and minor phases are revealed through the TEM diffraction patterns, specifically that both phases have the HCP crystal structure. The determined lattice parameters, Table 2, are nearly identical, within $\pm$ 0.01$\AA$, corroborating the previous findings from XRD and EBSD analyses.

The elemental maps obtained by scanning transmission electron microscopy (STEM), as shown in Fig. 4, further confirm that the minor phase is enriched in Ti and significantly depleted in Sc. These elemental maps also indicate a slight depletion of Hf and Zr in the minor phase.

3.2. Tracer diffusion measurements

The self-diffusion rates of the ^{89}Zr, ^{44}Ti, and ^{46}Sc radioisotopes in the HfScTiZr alloy were determined in the temperature range of 973 K to 1373 K. The experimental conditions used in the present experiments correspond to the thin film solution of the diffusion problem,

$$C(x,t) = \frac{M}{\sqrt{\pi D_v t}} \exp\left(-\frac{x^2}{4D_v t}\right). \quad (3)$$

Here, $C(x,t)$ is the concentration (relative specific activity) of the tracer elements viz., ^{89}Zr, ^{44}Ti, and ^{46}Sc at the corresponding diffusion depth x from the surface of the sample, t is the diffusion annealing time, D_v is the volume diffusion coefficient, and M is the initial amount of the tracer solution.

In the present case of diffusion in a polycrystalline material, grain boundary (GB) diffusion affects the penetration profiles. The so-called B-type kinetic regime of GB diffusion after Harrison's classification [46] has to be considered. By incorporating the Le Claire analysis [47] of the exact Suzuoka solution [48] for the GB diffusion problem, it is possible

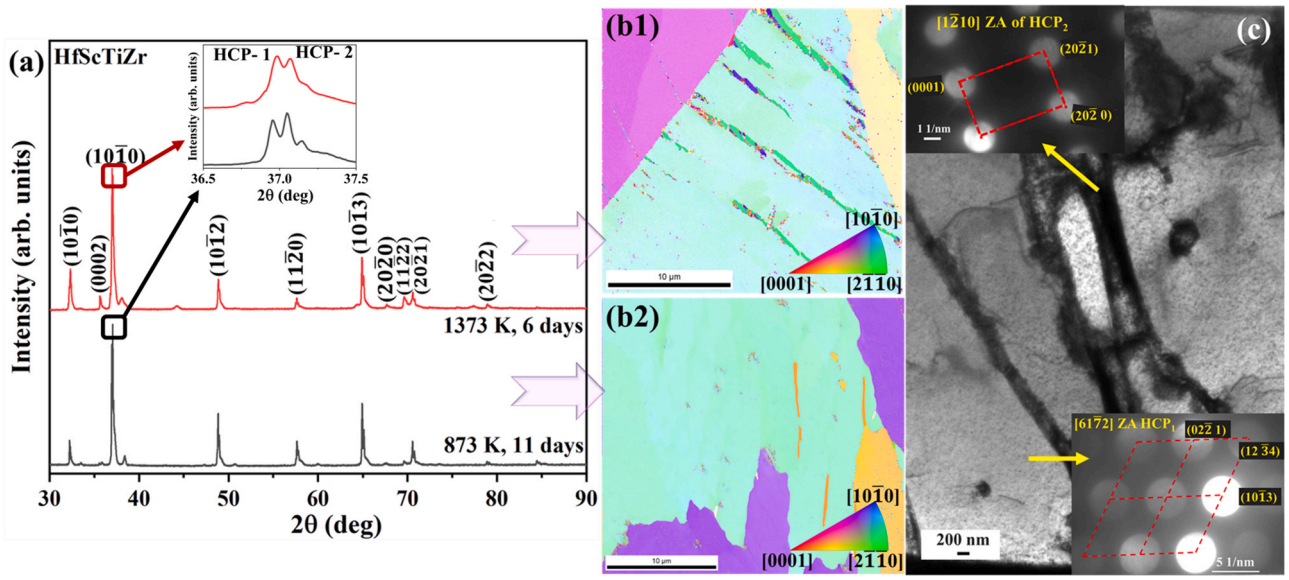

Fig. 3. Phase and microstructural characterization of the HfScTiZr HEA heat treated at 1373 K and 873 K: (a) XRD patterns; (b1) and (b2) EBSD results showing a random orientation of the grains in the microstructure; (c) TEM bright-field micrograph of the HfScTiZr alloy heat treated at 1373 K for 6 days, resolving the presence of two distinct and stable HCP phases. A slow-scan XRD analysis resolves the existence of the two HCP phases; see insert in (a).

Table 2
Lattice constants of the major and minor phases observed in the HfScTiZr alloy.

Phase	a (Å)	c (Å)
Major	3.198	5.042
Minor	3.184	5.021

to fit the penetration profiles as a combination of bulk and GB diffusion contributions,

$$C(x,t) = \frac{M}{\sqrt{\pi D_v t}}\exp\left(-\frac{x^2}{4D_v t}\right) + C^0_{gb}\exp(-Ax^{6/5}). \quad (4)$$

In the above equation, the second term represents the GB diffusion contribution, and C^0_{gb} and A are constants. The parameter C^0_{gb} is inversely proportional to the grain size d, i.e. $C^0_{gb} \propto \frac{\delta}{d}$. The parameter A determines the value of the so-called triple product, P, $P = s\delta D_{gb}$ [45]. Here, s is the segregation factor, and δ is the diffusional grain boundary width.

The penetration profiles measured for the diffusion of the ^{89}Zr, ^{44}Ti and ^{46}Sc radioisotopes are shown in Fig. 5(a), (b), and (c), respectively. Two distinct bulk and GB diffusion contributions are evident in almost all the profiles. The approximation of only two significant contributions corresponds exactly to the case of ^{89}Zr diffusion at the highest temperatures of 1373 K and 1273 K, Fig. 5(a). However, in the case of ^{46}Sc diffusion, two distinct volume diffusion branches (in addition to a contribution of the GB diffusion at large depths) are found in Fig. 5(c). In the case of diffusion of ^{44}Ti and ^{89}Zr, two volume diffusion contributions become prominent at lower temperatures, Fig. 5(a) and (b). The presence of two volume diffusion contributions can be attributed to the existence of two interconnected HCP phases due to the lamellar structure, as shown in Fig. 1, which provides parallel diffusion paths.

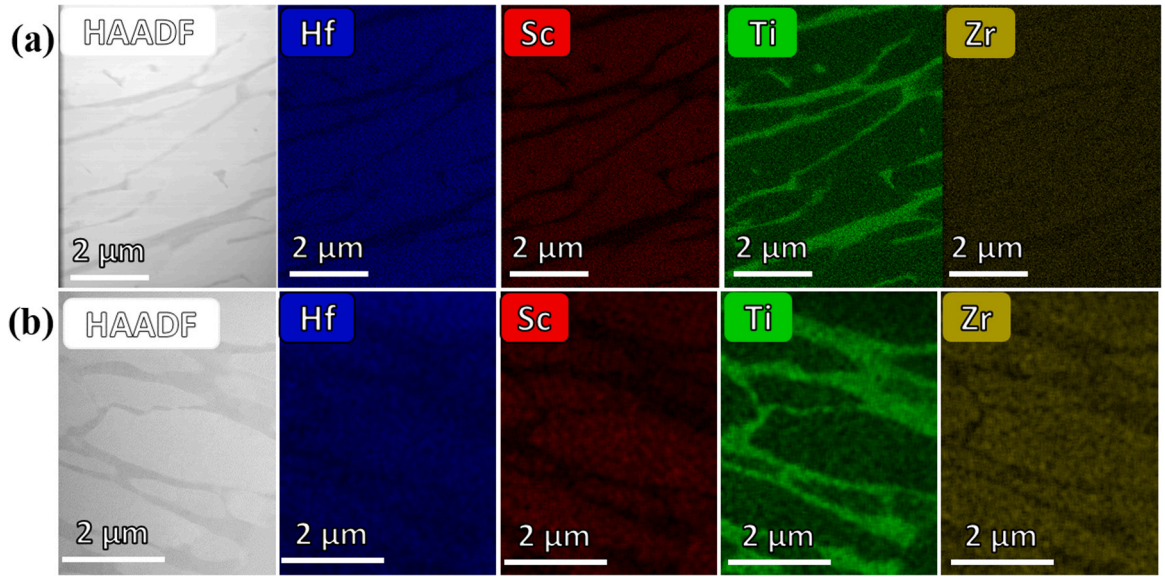

Fig. 4. HAADF-STEM images and the corresponding elemental maps of the HfScTiZr alloy heat treated for (a) 6 days at 1373 K and (b) 11 days at 873 K showing the elemental distribution in the major (Sc-rich) and minor (Ti-rich) phases.

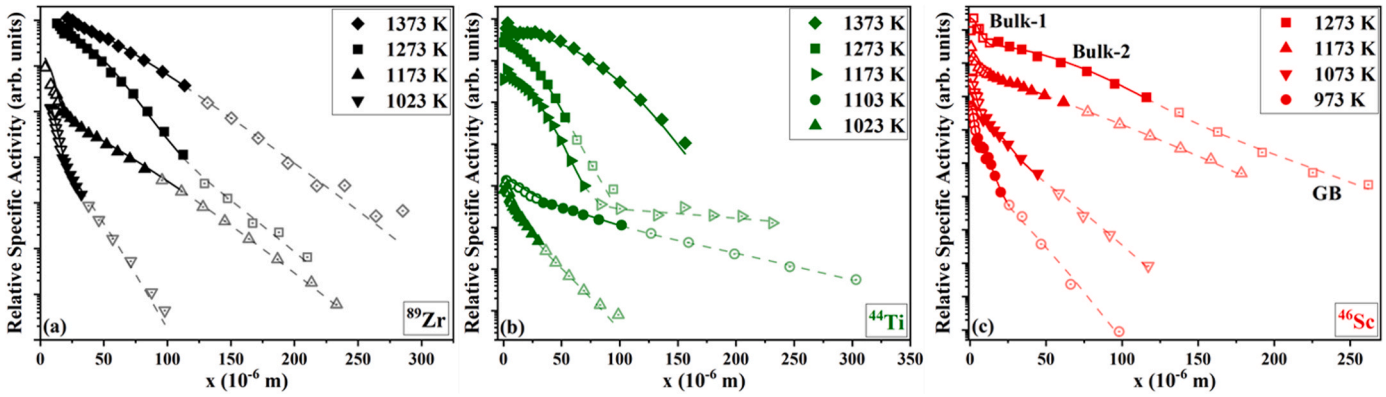

Fig. 5. Penetration profiles for the diffusion of (a) ^{89}Zr, (b) ^{44}Ti and (c) ^{46}Sc radiotracers in HfScTiZr. The open and closed symbols in the penetration profiles represent the relatively slow and fast contributions of the bulk tracer diffusion, respectively. The open symbols with dots represent the contribution of grain boundary diffusion (at large depths).

Such profiles can be approximated using a sum of two Gaussian solutions and the Le Claire solution [47]. Note that the second volume diffusion contribution for diffusion of Zr and Ti can be clearly distinguished only at lower temperatures, and the number of data points is insufficient for a reliable estimation of the Arrhenius parameters. The direct implantation of the ^{46}Sc tracer probably helps to separate the two contributions of the volume diffusion reliably from the penetration profiles. The determined diffusion coefficients are listed in Table 3.

A short note is due here. Three types of short circuits may potentially contribute to diffusion, i.e., high-angle GBs in both HCP phases and the phase boundaries. In view of the specific microstructure, Fig. 1(b), the high-angle GBs form only short segments and cannot provide diffusional transport over hundreds of micrometers, as observed for the penetration profiles shown in Fig. 5. The phase boundaries correspond predominantly to low-angle interfaces with almost negligible misfit between the two lattices. One may safely argue that the corresponding diffusivities of the phase boundaries are low and cannot be resolved in the present experimental conditions. We thus conclude that the GB contribution to the diffusion profiles is due to high-angle GBs in the major HCP phase, which likely determine the deep tracer penetration as in Fig. 5. Still, the GB diffusion contribution in Eq. (4), with additionally accounting for a second volume diffusion contribution, if required, is estimated to describe the volume diffusion data correctly. It is important to note that the current experimental conditions were not specifically designed or optimized for conducting GB diffusion measurements. Thus, the corresponding data concerning GB diffusion were not evaluated.

Table 3
Temperature T, time t of the tracer diffusion experiments, and the determined diffusion coefficients of Ti, Zr, and Sc in HfScTiZr. Two diffusion coefficients, D_{slow} and D_{fast}, if resolved, are reported for each tracer. The typical experimental uncertainties of the determined tracer diffusion coefficients do not exceed 20 %.

T(K)	t(10^4 s)	D^{Ti}_{fast} (10^{-15} m^2/s)	D^{Ti}_{slow}	D^{Sc}_{fast}	D^{Sc}_{slow}	D^{Zr}_{fast}	D^{Zr}_{slow}
1373	0.36	251	–	–	–	332	–
1323	0.36	105	–	–	–	–	–
1273	0.36	47.3	–	90	1.98	73.6	–
1173	8.64	7.45	–	–	–	6.01	2.89
1173	7.20	–	–	5.97	0.263	–	–
1103	43.02	2.30	0.433	–	–	–	–
1073	69.12	–	–	0.144	0.00973	–	–
1023	17.28	0.367	0.0517	–	–	–	–
1023	69.21	–	–	–	–	0.259	0.0358
973	163.26	–	–	0.0172	0.001	–	–

4. Discussion

4.1. Phase stability of the HfScTiZr alloy and Theoretical predictions

A high compositional and microstructural stability of the major and minor HCP phases is affirmed by comparison of the homogenized and heat-treated samples, Figs. 1 and 3. The line scans obtained from the HAADF-STEM EDS analysis are shown in Fig. S3 in Supplementary Material, and the composition variations along and across the Ti-rich phase are compared. The chemical compositions are relatively constant within each phase, and no local/atomic level segregation is observed at the phase boundaries.

The DFT-based chemical potential calculations by Zhang et al. [34] revealed that the Sc and Ti chemical potentials for the HfScTiZr equiatomic composition (assuming a single-phase HCP structure) are higher than those in binary HfZr or ternary HfTiZr alloys. We conclude that adding Sc and Ti increases the Gibbs free energy of the system, which might potentially promote phase separation. Additionally, the miscibility gap in the binary Ti–Sc system [49] further promotes such phase separation. Examining the elemental impact on observed phase separation can be better comprehended through a thorough investigation employing phase field simulations [50].

Accounting for the calculated 0 K mixing energy and the ideal configurational entropy, the free energy difference between the equiatomic HCP solid solution and a two-phase mixture of Sc- and Ti-rich HCP phases was determined, Fig. 6. The experimentally determined phase fractions f and compositions of the two HCP phases were used as input for the DFT calculations, see Eq. (1). In view of the given limits of the accuracy of experimental data with respect to both chemical composition and phase fractions, the calculations were performed for two data sets of different compositions to provide a sensitivity check of the current predictions. Moreover, minor composition adjustments were necessary to align with the total number of atoms per supercell. Please refer to Table S-I in the Supplementary Material for details.

Fig. 6 substantiates that even slight modifications of the composition within 2–3 at % result in a significant variation of the decomposition temperature. The free energy difference suggests that the two-phase mixture is stable below 571 K (set-1) or below 1191 K (set-2). The discrepancy with the experimental results (two co-existing HCP phases below 1373 K) can mainly be attributed to the fact that the DFT-informed calculations were performed without accounting for thermal excitations (vibrational and electronic as well as their coupling effect) and/or potential short-range order which may have an impact on both mixing enthalpy and configurational entropy. Preliminary atomic resolution images using high-resolution STEM indicate local ordering in the Ti-rich minor phase. To fully incorporate these missing contributions, advanced simulation techniques, such as full finite-temperature free

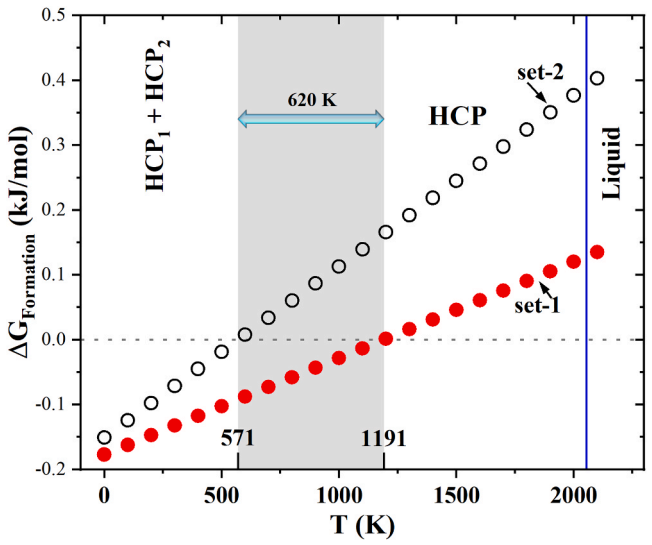

Fig. 6. Free energy difference between a single HCP solid solution and the two-phase mixture of Sc-rich and Ti-rich HCP phases in HfScTiZr calculated by DFT. The set #1 and set #2 are specified in the Supplementary Material.

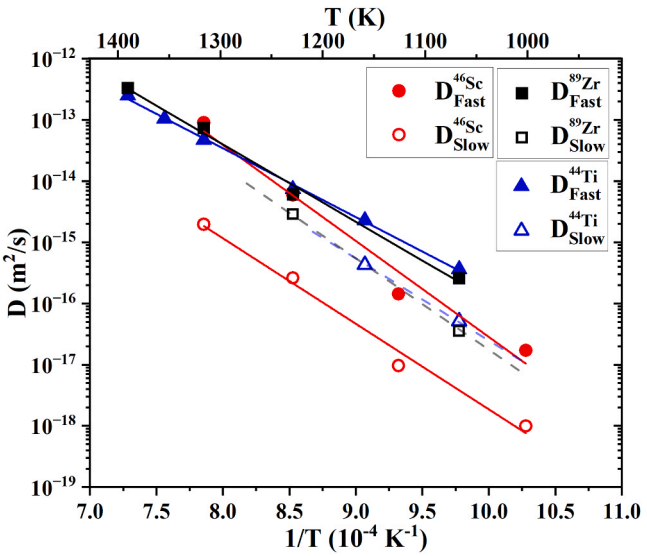

Fig. 7. Arrhenius plot for self-diffusion of alloying elements in HfScTiZr. The closed symbols represent the fast diffusivities, and the open symbols correspond to the slow diffusivities.

energy calculations [51], are generally required. The short-range order effects can be via, e.g., the *ab initio*-based cluster expansion technique [25,52,53] in conjunction with the Monte Carlo method. These simulations are, however, computationally very demanding and beyond the scope of the present work.

Note that the CALPHAD calculations presented in Fig. 2 underestimate the decomposition temperature, too. A careful analysis of the thermodynamic database used for the CALPHAD calculations indicates an issue with the Sc–Ti binary phase diagram. Two different phase diagrams were available for Sc–Ti in the early 1960 s, one from Beaudry et al. [54] and another from Savitskii et al. [55]. The phase diagram from Savitskii et al. [55] was not adopted in the later studies [56,57] due to elemental purity issues in the experiments considered in [55]. However, in the TCAL7 database, the phase diagram from [55] is considered as evident from the calculated Sc–Ti phase diagram using the TCAL7 database (Fig. S1a) in the Supplementary file. The diagram from [56] is given for comparison (Fig. S1b). Even the assessed Gibbs energy descriptions of the Sc–Ti system from [57] have significant discrepancies compared to the experiments as indicated by [56]. The prevailing investigation also highlights a compelling necessity for further improving the thermodynamic assessment of the Sc–Ti binary and higher-order systems that contain Sc–Ti.

The impact of thermodynamic quantities on the phase stability is exemplified by CALPHAD calculations at 873 K. The enthalpy of mixing for the single phase HCP with the composition equal to that of the observed overall composition of the alloy is 2532 J/mole. This value is determined by forcing stability of a single HCP phase by the local equilibrium calculations in Thermo-Calc. When actual (global) equilibrium calculations are performed, two HCP phases appear, and the enthalpy of mixing decreases to 1115 J/mole. Thus, the phase separation reduces the enthalpy of mixing at low temperatures. The CALPHAD-predicted compositions of the HCP phases are compared with the experimental results in Table 1.

4.2. Tracer diffusivities in the HfScTiZr alloy

The high thermal stability of the two-phase mixture observed after prolonged heat treatments ensures the reliability of the diffusion measurements in the HfScTiZr alloy.

The Arrhenius dependencies for the estimated volume diffusivities of Zr, Ti, and Sc are shown in Fig. 7. Both fast (filled symbols) and slow (open symbols) contributions are reported. The resulting Arrhenius parameters, Q and D_0, are listed in Table 4.

Fig. 7 suggests that Sc is the slowest diffusing element, while Zr and Ti reveal similar (and faster) diffusivities. Furthermore, two (volume) diffusion contributions are seen for all elements, with the largest difference between the diffusivities observed for the slow diffusing element, i.e., Sc. While the difference of Sc diffusivities in the two HCP phases exceeds an order of magnitude, such differences for Ti and Zr amount to less than an order of magnitude at the lowest temperature, and they disappear at higher temperatures above 1300 K, Fig. 7.

In view of the specific microstructure, Fig. 1(b), we assume that the two HCP phases provide the two volume diffusion contributions. The vacancy formation and migration energies depend on the alloy composition, especially the chemistry around a vacancy. Previous DFT-based calculations [34] revealed that the vacancy formation energies increase with an increase in the number of Ti atoms around a vacancy and decrease with an increase in the number of Sc atoms around a vacancy. Thus, one may safely assume that Sc diffusion in the Sc-rich (major) phase is faster than in the Sc-lean (minor) phase. Since the vacancy concentration decreases with increasing Ti concentration, diffusion of both Ti and Zr are probably retarded in the Ti-rich (minor) phase. This reasoning allows us to interpret the "fast" contributions as those corresponding to diffusion in the major, Sc-rich phase, while the "slow" diffusivities are likely to represent the diffusion parameters in the Ti-rich, minor phase of the HfTiZrSc system.

In the below sections, the estimated diffusivities of Zr, Sc and Ti are compared within different HCP matrices on both absolute and homologous temperature scales, Figs. 8, 9 and 10.

4.2.1. Zr diffusion

The data of Zr self- and impurity diffusivities in the relevant pure

Table 4
Activation enthalpies, Q, and pre-exponential factors, D_0, for self-diffusion in HfScTiZr. Two volume diffusion contributions, denoted as "fast" and "slow", are distinguished.

Tracer	Q(kJ/mol)	D_0(m^2/s)	Remark
Zr	242 ± 14	$5.27^{+62}_{-1.07} \times 10^{-4}$	"fast"
Ti	215 ± 5	$3.42^{+14.6}_{-0.86} \times 10^{-5}$	"fast"
Sc	300 ± 33	$0.14^{+105}_{-0.13}$	"fast"
Sc	267 ± 20	$17.61^{+615}_{-8.3} \times 10^{-5}$	"slow"

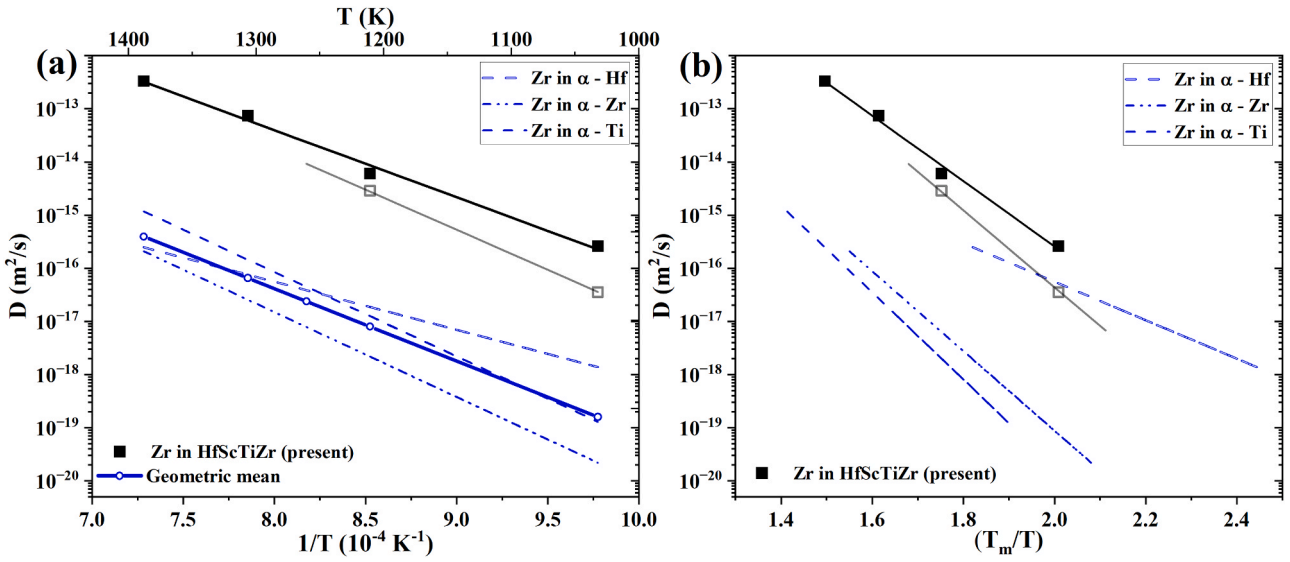

Fig. 8. Arrhenius plots for Zr diffusion in various HCP metals and the present HfScTiZr alloy showing a comparison on (a) the inverse absolute temperature scale and (b) the inverse homologous temperature scale. The plots show the comparison of the present experimental data with the available literature data on Zr diffusion in pure α-Ti [59] (short dashed line), α-Zr [61] (dotted-dashed line), and α-Hf [58] (dashed line). The closed symbols connected by a solid line represent the fast diffusivities, and the open symbols represent the estimated slow diffusivities. The thick solid line in (a) represents the calculated geometric mean of the diffusivities, Eq. (5).

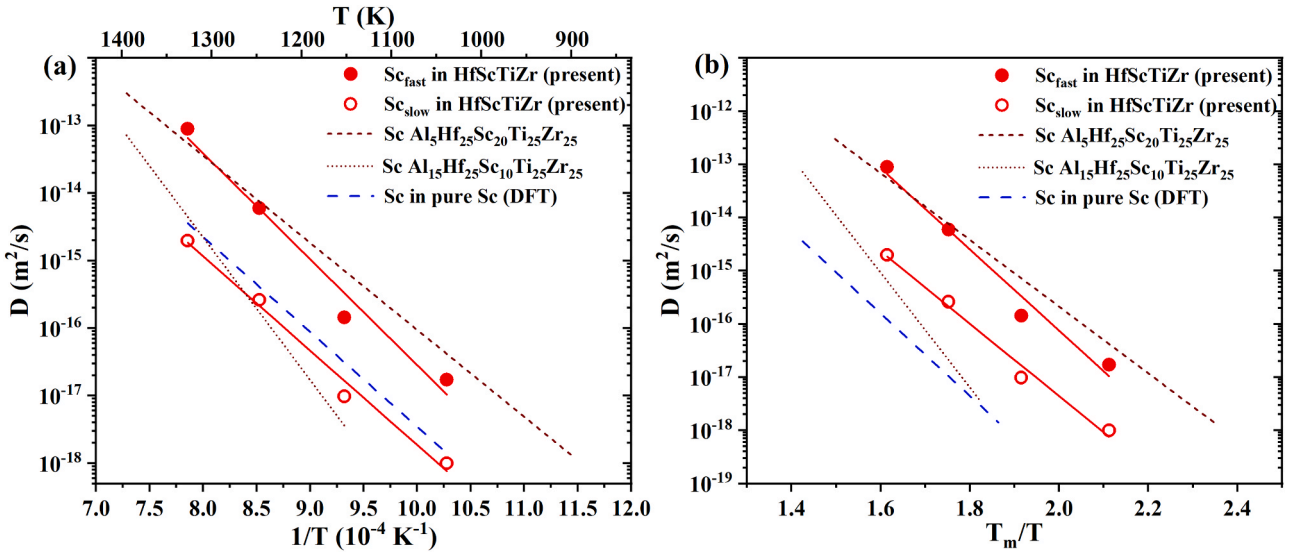

Fig. 9. Arrhenius plots for Sc diffusion in the HfScTiZr alloy in comparison with pure Sc [62] (blue dashed line) on (a) the inverse absolute temperature scale and (b) the inverse homologous temperature scale. The closed symbols connected with solid lines represent the fast diffusivities and the open symbols represent the estimated slow diffusivities in HfScTiZr. The Sc diffusivities in $Al_5Hf_{25}Sc_{20}Ti_{25}Zr_{25}$ (short dashed line) and $Al_{15}Hf_{25}Sc_{10}Ti_{25}Zr_{25}$ (dotted line) are taken from Ref. [58].

elements are available, and they are compared with the present data on Zr diffusion in the HfScTiZr alloy in Fig. 8. The Zr diffusion rate is significantly increased in the multi-principal element matrix (HfScTiZr) with respect to the Zr diffusivities in the unary HCP metals by two to three orders of magnitude. This trend holds even when the data is compared on the homologous temperature scale, especially for pure Ti and Zr. The Zr diffusion rates in the multi-component alloy are significantly larger, by about three orders of magnitude, than the geometric mean of the Zr diffusivities in the pure elements, Fig. 8(a).

Note that the geometric mean, $\overline{D}^{Zr}$, shown in Fig. 8 has been estimated using the available data for Zr diffusion in pure α-Hf (D^{Zr}_{Hf}) [58], α-Ti (D^{Zr}_{Ti}) [59] and α-Zr (D^{Zr}_{Zr}) [60] as:

$$\overline{D}^{Zr} = \left(D^{Zr}_{Hf} \cdot D^{Zr}_{Ti} \cdot D^{Zr}_{Zr}\right)^{1/3}, \quad (5)$$

since experimental data on Zr diffusion in pure Sc are not available.

4.2.2. Sc Diffusion

The comparison of Sc diffusivities in the HfScTiZr alloy with the Sc diffusion rates in $Al_5Hf_{25}Sc_{20}Ti_{25}Zr_{25}$ and $Al_{15}Hf_{25}Sc_{10}Ti_{25}Zr_{25}$ [58] is presented in Fig. 9. To the best of our knowledge, experimental investigations on diffusion in pure Sc are absent, probably because of its high reactivity and highly volatile nature, which releases carcinogenic fumes. So, the DFT-based predictions of the Sc self-diffusivity [62] are considered for the comparison.

On the absolute temperature scale, Fig. 9(a), the "fast" diffusivities of

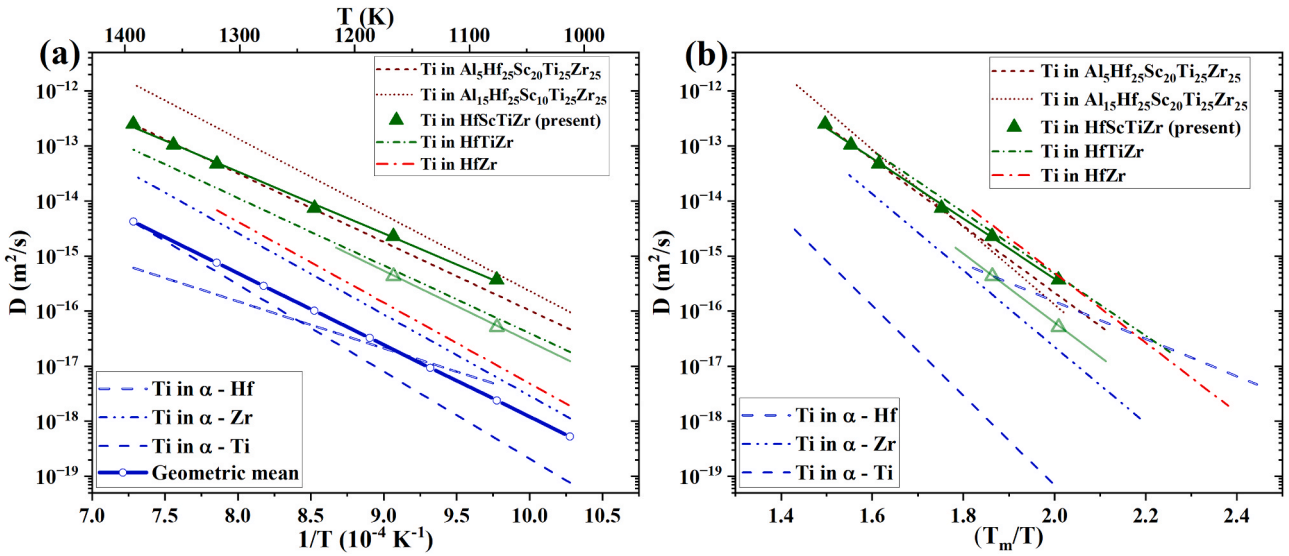

Fig. 10. Arrhenius plots for Ti diffusion in various HCP systems showing a comparison on (a) the inverse absolute temperature scale and (b) the inverse homologous temperature scale. The plots show the comparison of the present experimental data with the available literature data on Ti diffusion in pure α-Ti [63] (blue dashed line), α-Zr [60] (blue dot-dashed line), α-Hf [21] (blue short dashed line), and HCP alloys [21]. The closed symbols connected by solid lines represent the fast diffusivities and the open symbols represent the estimated slow diffusivities. The thick solid line in (a) represents the estimated geometric mean of the Ti diffusivities in unaries.

Sc in HfScTiZr, i.e., presumably Sc diffusion coefficients in the Sc-rich phase, are similar to those in (Sc-enriched) $Al_5Hf_{25}Sc_{20}Ti_{25}Zr_{25}$. On the other hand, the "slow" diffusivities in HfScTiZr, i.e., presumably Sc diffusion coefficients in the Sc-lean phase, are similar to those in (relatively Sc-lean) $Al_{15}Hf_{25}Sc_{10}Ti_{25}Zr_{25}$ and do not strongly deviate from DFT predictions for pure Sc. This comparison suggests that Al probably has little impact on the diffusion kinetics in the AlHfScTiZr system. This comparison confirms our interpretation of the "slow" and "fast" diffusivities in the two-phase HfScTiZr system strongly as diffusion in the Sc-rich and Sc-lean phases, respectively.

4.2.3. *Ti Diffusion*

In Fig. 10(a) and (b), the Ti diffusivities in the HfScTiZr multicomponent alloy are compared with literature data on Ti diffusion in HCP α-Hf [21], α-Zr [60] and α-Ti [63] and other HCP alloys [21] on absolute and homologous temperature scales, respectively. The Ti diffusion rates are found to increase on the absolute temperature scale with an increasing number of elements in the alloy. (The geometric mean for Ti diffusion was determined similarly to Eq. (5).) Ti diffusion in the four-component HfScTiZr and five-component AlHfScTiZr HEA exceeds the geometric mean of the Ti diffusivities in the corresponding unaries by several orders of magnitude. This behavior clearly contradicts the original hypothesis on "sluggish" diffusion in HEAs [17] and strongly supports the recently reported "anti-sluggish" behavior observed for HCP HEAs [21].

On the homologous temperature scale, this behavior is more peculiar. Ti diffusion in binary HfZr is slightly faster as in HfScTiZr, but Ti diffusivities in unaries are significantly lower, Fig. 10(b). Generally, Ti diffusion rates in these HCP alloys are found to be similar on the homologous temperature scale.

4.2.4. *General trends in diffusivities*

The present results for the four-component HfScTiZr alloy further confirm the previous findings for the five-component AlHfScTiZr HEAs [21] on the "anti-sluggish" character of tracer diffusion rates with respect to the chemical complexity of these HCP HEAs. The diffusion enhancement is obvious on the absolute temperature scale, but it remains spectacular on the homologous temperature scale as well. Thus, a moderate decrease of Gibbs free energy by increasing the configurational entropy is not sufficient to generalize the diffusion behavior in multi-principal element alloys, as it was reported previously [23,25]. In fact, the element interactions, lattice distortions, and potential ordering around vacancies need to be accounted for as these determine the diffusion behavior.

In general, potential energy fluctuations (PEFs) representing the atomic interactions, including both elastic and chemical contributions in the lattice, were suggested to influence vacancy-mediated diffusion in HEAs [64]. In Fig. S2 of the Supplementary Material, Ti and Sc diffusion coefficients are plotted against the potential energy fluctuations. While a linear increase of the Ti diffusion rate with increasing value of PEFs is seen, the Sc diffusivity shows a rather non-monotonous behavior, suggesting that PEF are probably not a suitable parameter to quantify the diffusion rates in HEAs. Note that the increase of the Ti diffusion coefficients with increasing PEFs contradicts the main premise of "sluggish" diffusion as a core effect in HEAs.

The "sluggish" diffusion concept in HEAs was postulated considering the impact of varying energy barriers on vacancy migration due to fluctuating local environments [2]. Later, the lattice distortions were considered important in influencing the diffusional properties in non-FCC lattices [65]. Recently, the element-specific lattice distortions or mean squared atomic displacements were found to be one of the decisive parameters [20].

Thus, the DFT-calculated MSADs (element-specific quantities) were analyzed to quantify the diffusion behavior in the present HCP HEAs. The determined MSADs with respect to the particular lattice sites in the major and minor phases of HfScTiZr are shown in Fig. 11(a) and compared to the literature data on MSADs in other HCP matrices [21]. The MSADs in the HfScTiZr alloy forming a hypothetical single phase are also given to demonstrate the influence of the observed phase and its composition. Fig. 11(a) substantiates a huge difference in the calculated MSADs in different phases, indicating the importance and sensitivity of the chemical composition of the alloy/phase.

The MSAD values in the major (Sc-rich) HfScTiZr phase are very similar, especially for Ti and Zr. This finding correlates with the similarity of the measured tracer diffusivities of Zr and Ti. Slightly lower diffusivity of Sc in this phase with respect to the diffusion rates of Ti and Zr, Fig. 7, correlates with lower values of the MSAD for Sc.

The "fast" diffusion coefficients of Ti and Sc in HfScTiZr at a fixed

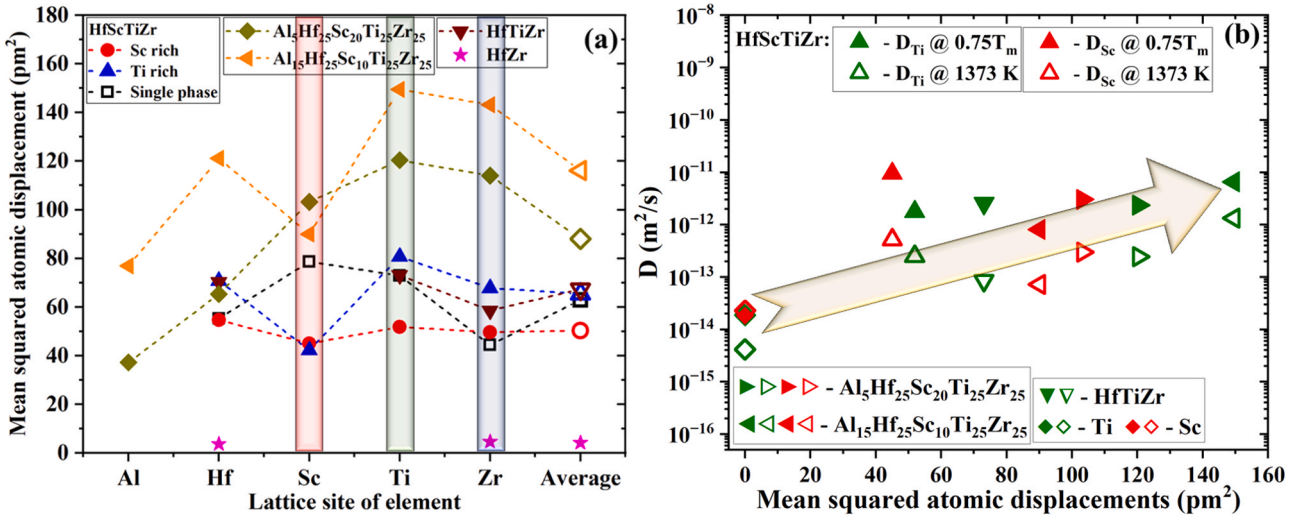

Fig. 11. (a) Mean-squared atomic displacements (MSADs) with respect to the lattice positions in the equilibrium lattice calculated for the Sc-rich and Ti-rich HCP phases and for a random HCP solid solution in HfScTiZr in comparison to the data for other HCP phases [21]. (b) Tracer diffusion coefficients of Ti (green symbols) and Sc (red symbols) as measured at a fixed absolute temperature of 1373 K (open symbols) and fixed homologous temperature of $0.75T_m$ (filled symbols) plotted against the corresponding MSADs. The arrow in (b) indicates an anticipated trend.

absolute temperature of 1373 K and at a fixed homologous temperature $0.75T_m$, corresponding presumably to the Sc-rich phase in this alloy, are plotted against the MSAD values in Fig. 11(b). These diffusion rates are also compared to the values measured for other HCP matrices at the same (absolute and homologous) temperatures. Fig. 11(b) indicates a common trend for the measured tracer diffusion coefficients. In fact, the diffusion coefficients of Ti and Sc are generally increase with an increase of MSADs. The Sc diffusion coefficients measured in the Sc-rich HfScTiZr phase somewhat deviate from the common trend. Note that all other materials reveal a stable single phase corresponding to an HCP solid solution.

Hence, the diffusion behavior in the present HCP alloys is predominantly influenced by the site-specific lattice distortions (MSADs) and the chemical interactions of the constituent alloying elements. Generally, the configurational entropy will increase with increasing number of elements, irrespective of their nature. However, the MSADs (lattice distortions) vary depending on the interactions within the alloying elements and correlate with the diffusion behavior in the lattice.

To further advance the understanding of the general diffusivity trends, a more elaborate theoretical analysis of multi-component diffusion is required, utilizing, for example, the rapidly evolving machine-learning-supported simulation techniques[68]. Among these, a highly efficient *ab initio* method, the transition state thermodynamic integration (TSTI) approach [66], has been very recently developed by making use of machine-learning interatomic potentials [67]. The TSTI approach enables the efficient computation of the Gibbs energy at the transition state with DFT accuracy, addressing the inherent dynamical instability that hinders the application of standard thermodynamic integration methods. In combination with the above-mentioned full finite-temperature free energy calculations [51], the *ab initio*-determined absolute values of the diffusion coefficients are in reach even for chemically complex alloys such as the investigated HfScTiZr alloy in the present study.

5. Conclusion

The microstructural stability and the self-diffusion behavior of the HfScTiZr multi-principal-element alloy have been investigated in-depth. Self-diffusion rates of ^{44}Ti, ^{46}Sc, ^{89}Zr have been measured using the radiotracer diffusion technique, and the Arrhenius parameters for the diffusion have been determined. The major conclusions from the current investigation are as follows: .

- The quaternary HfScTiZr alloy exhibits two different HCP phases with almost similar lattice parameters. The major HCP phase is rich in Sc with lattice constants a = 3.198Å, c = 5.042Å and the minor phase is rich in Ti with lattice constants a = 3.184Å, c = 5.021Å. Both phases are found to be extremely stable even after prolonged heat treatments.
- The existing CALPHAD database is insufficient to predict the HfScTiZr alloy's phase stability due to the lack of a reliable database for the binary Sc–Ti system, highlighting the need for further investigations.
- The diffusivities of ^{44}Ti, ^{46}Sc, ^{89}Zr follow Arrhenius-type temperature dependencies.
- Two distinct volume diffusion contributions (slow and fast) are present in the penetration profiles of the radiotracers. The slow contribution of the ^{46}Sc diffusion can be conveniently extracted at all temperatures under investigation while the second contribution is only separable at low temperatures in the penetration profiles of ^{44}Ti and ^{89}Zr diffusion. The present analysis indicates that the distinct diffusion contributions result from the Sc-rich major (fast diffusivities) and Ti-rich minor (slow diffusivities) HCP phases. The vacancy formation energies reported in the literature [34] further support the present analysis.
- The site/element-specific lattice distortions (MSADs) obtained from DFT calculations present an appropriate parameter to explain the diffusion behavior. Both Ti and Sc diffusivities increase with an increase of the MSAD value.
- Finally, the anticipated sluggish diffusion with increasing configurational entropy is not observed for the present HCP multicomponent alloys. Rather, an "anti-sluggish" diffusion behavior is prominent.

CRediT authorship contribution statement

Blazej Grabowski: Software, Writing – review & editing. **Sergiy V. Divinski:** Conceptualization, Formal analysis, Methodology, Supervision, Writing – review & editing. **G. Mohan Muralikrishna:** Conceptualization, Data curation, Formal analysis, Investigation, Methodology, Writing – original draft, Writing – review & editing. **Gerhard Wilde:** Resources, Supervision, Writing – review & editing. **Sai Kumaran Ayyappan:** Investigation. **Sandipan Sen:** Investigation. **K.**

Guruvidyathri: Software, Writing – review & editing. **Shanmugam Sankaran:** Investigation, Writing – review & editing. **Lukasz Rogal:** Investigation, Writing – review & editing. **Juliana Schell:** Investigation, Resources. **Joachim Mayer:** Formal analysis. **Xi Zhang:** Software, Writing – review & editing.

Declaration of Competing Interest

The authors declare that they have no known competing financial interests or personal relationships that could have appeared to influence the work reported in this paper.

Data availability

Data will be made available on request.

Acknowledgements

G.M.M. acknowledges the Alexander von Humboldt (AvH) Foundation for awarding a Fellowship to conduct research at the Institute of Materials Physics, University of Münster, Germany. Financial support from the Deutsche Forschungsgemeinschaft (DFG) via the research projects DI 1419/24-1 and ZH 1218/1-1 is gratefully acknowledged. X. Z. and B.G. acknowledge the support by the state of Baden-Württemberg through bwHPC and the German Research Foundation (DFG) through grant No. INST 40/575-1 FUGG (JUSTUS 2 cluster) and by the Stuttgart Center for Simulation Science (SimTech). We acknowledge the support of the European Union's Horizon Europe Framework research and innovation programme under grant no. 101057511 (EURO-LABS) and of the European Union's Horizon 2020 Framework Research and Innovation Program under grant agreement no. 654002 (ENSAR2) and grant agreement no. 865855 (Materials 4.0). The DFG is further acknowledged for funding the TEM equipment at the University of Münster via the Major Research Instrumentation Program under INST 211/719-1 FUGG. The authors acknowledge the Central Facility for Electron Microscopy (RWTH Aachen) for support and access to their FIB facilities. We acknowledge the financial support received from the Federal Ministry of Education and Research (BMBF) through grants 05K16PGA and 05K22PGA. We also acknowledge the support of all the technical teams at ISOLDE for their excellent work in delivering high-quality beams for diffusion measurements.

Appendix A. Supporting information

Supplementary data associated with this article can be found in the online version at doi:10.1016/j.jallcom.2023.173196.

References

[1] E.P. George, W. Curtin, C.C. Tasan, High entropy alloys: a focused review of mechanical properties and deformation mechanisms, Acta Mater. 188 (2020) 435.
[2] J.W. Yeh, S.K. Chen, S.J. Lin, J.Y. Gan, T.S. Chin, T.T. Shun, C.H. Tsau, S.Y. Chang, Nanostructured high-entropy alloys with multiple principal elements: novel alloy design concepts and outcomes, Adv. Eng. Mater. 6 (2004) 299.
[3] D.B. Miracle, High-entropy alloys: a current evaluation of founding ideas and core effects and exploring "nonlinear alloys", Jom 69 (2017) 2130.
[4] Y. Lu, Y. Dong, H. Jiang, Z. Wang, Z. Cao, S. Guo, T. Wang, T. Li, P.K. Liaw, Promising properties and future trend of eutectic high entropy alloys, Scr. Mater. 187 (2020) 202.
[5] G.M. Muralikrishna, A.C.M. Esther, K. Guruvidyathri, P. Watermeyer, C. H. Liebscher, K.N. Kulkarni, G. Wilde, S.V. Divinski, B.S. Murty, Novel multicomponent B2-ordered aluminides: compositional design, synthesis, characterization, and thermal stability, Metals 10 (2020) 1411.
[6] J. Fang, J. Wang, Y. Wang, H. He, D. Zhang, Y. Cao, Microstructure evolution and deformation behavior during stretching of a compositionally inhomogeneous TWIP-TRIP cantor-like alloy by laser powder deposition, Mater. Sci. Eng.: A 847 (2022), 143319.
[7] J. Hu, K. Yang, Q. Wang, Q.C. Zhao, Y.H. Jiang, Y.J. Liu, Ultra-long life fatigue behavior of a high-entropy alloy, Int. J. Fatigue (2023), 108013.
[8] H. Hamdi, H.R. Abedi, Y. Zhang, A review study on thermal stability of high entropy alloys: normal/abnormal resistance of grain growth, J. Alloy. Compd. (2023), 170826.
[9] M.M. Garlapati, M. Vaidya, A. Karati, S. Mishra, R. Bhattacharya, B. Murty, Influence of Al content on thermal stability of nanocrystalline Al_xCoCrFeNi high entropy alloys at low and intermediate temperatures, Adv. Powder Technol. 31 (2020) 1985.
[10] R. Bhattacharya, M. Annasamy, P. Cizek, M. Kamaraj, G.M. Muralikrishna, P. Hodgson, D. Fabijanic, B. Murty, Evolution of phase constitution with mechanical alloying and spark plasma sintering of nanocrystalline Al_xCoCrFeNi (x = 0, 0.3, 0.6, 1 mol) high-entropy alloys, J. Mater. Res. 37 (2022) 959.
[11] A. Hussain, R. Dhaka, H.J. Ryu, S.K. Sharma, P.K. Kulriya, A critical review on temperature dependent irradiation response of high entropy alloys, J. Alloy. Compd. (2023), 169624.
[12] B.R. Anne, S. Shaik, M. Tanaka, A. Basu, A crucial review on recent updates of oxidation behavior in high entropy alloys, SN Appl. Sci. 3 (2021) 1.
[13] Q. Guo, H. Hou, Y. Pan, X. Pei, Z. Song, P.K. Liaw, Y. Zhao, Hardening-softening of $Al_{0.3}$ CoCrFeNi high-entropy alloy under nanoindentation, Mater. Des. (2023), 112050.
[14] K. Wang, J. Zhu, H. Wang, K. Yang, Y. Zhu, Y. Qing, Z. Ma, L. Gao, Y. Liu, S. Wei, et al., Air plasma-sprayed high-entropy $(Y_{0.2}$ $Yb_{0.2}$ $Lu_{0.2}$ $Eu_{0.2}$ $Er_{0.2})_3$ Al_5 O_{12} coating with high thermal protection performance, J. Adv. Ceram. 11 (2022) 1571.
[15] B. Xing, Q. Ding, B. Jin, X. Zuo, N. Zhang, S. Yin, Corrosion resistance and passivation behavior of CoCrFeNi-TiAl high-entropy alloy coatings in acidic solutions, J. Therm. Spray. Technol. 31 (2022) 1673.
[16] H. He, J. Fang, J. Wang, T. Sun, Z. Yang, B. Ma, H. Chen, M. Wen, Carbide-reinforced Re0. 1Hf0. 25NbTaW0. 4 refractory high-entropy alloy with excellent room and elevated temperature mechanical properties, Int. J. Refract. Met. Hard Mater. 116 (2023), 106349.
[17] M.-H. Tsai, J.-W. Yeh, High-entropy alloys: a critical review, Mater. Res. Lett. 2 (2014) 107.
[18] M. Vaidya, K.G. Pradeep, B. Murty, G. Wilde, S. Divinski, Bulk tracer diffusion in CoCrFeNi and CoCrFeMnNi high entropy alloys, Acta Mater. 146 (2018) 211.
[19] J. Kottke, M. Laurent-Brocq, A. Fareed, D. Gaertner, L. Perrière, L. Rogal, S. V. Divinski, G. Wilde, Tracer diffusion in the Ni–CoCrFeMn system: Transition from a dilute solid solution to a high entropy alloy, Scr. Mater. 159 (2019) 94.
[20] J. Zhang, C. Gadelmeier, S. Sen, R. Wang, X. Zhang, Y. Zhong, U. Glatzel, B. Grabowski, G. Wilde, S.V. Divinski, Zr diffusion in BCC refractory high entropy alloys: a case of 'non-sluggish' diffusion behavior, Acta Mater. 233 (2022), 117970.
[21] S. Sen, X. Zhang, L. Rogal, G. Wilde, B. Grabowski, S.V. Divinski, 'Anti-sluggish' Ti diffusion in HCP high-entropy alloys: chemical complexity vs. lattice distortions, Scr. Mater. 224 (2023), 115117.
[22] S. Sen, X. Zhang, L. Rogal, G. Wilde, B. Grabowski, S.V. Divinski, Does Zn mimic diffusion of Al in the HCP Al-Sc-Hf-Ti-Zr high entropy alloys? Scr. Mater. 229 (2023), 115376.
[23] S.V. Divinski, A.V. Pokoev, N. Esakkiraja, A. Paul, A mystery of "sluggish diffusion" in high-entropy alloys: the truth or a myth? Diffus. Found. 17 (2018) 69.
[24] J. Dabrowa, M. Zajusz, W. Kucza, G. Cieślak, K. Berent, T. Czeppe, T. Kulik, M. Danielewski, Demystifying the sluggish diffusion effect in high entropy alloys, J. Alloy. Compd. 783 (2019) 193.
[25] A. Dash, A. Paul, S. Sen, S. Divinski, J. Kundin, I. Steinbach, B. Grabowski, X. Zhang, Recent advances in understanding diffusion in multiprincipal element systems, Annu. Rev. Mater. Res. 52 (2022) 383.
[26] G. Mohan Muralikrishna, M. Vaidya, B.S. Murty, S.V. Divinski, G. Wilde, Tracer diffusion in ordered pseudo-binary multicomponent aluminides, Scr. Mater. 178 (2020) 227.
[27] G.M. Muralikrishna, V.A. Esin, K.N. Kulkarni, B. Murty, G. Wilde, S.V. Divinski, Atomic transport in B2-ordered Al(Fe,Ni) alloys: tracer-interdiffusion couple approach, Intermetallics 126 (2020), 106920.
[28] J. Zhang, G.M. Muralikrishna, A. Asabre, Y. Kalchev, J. Müller, B. Butz, S. Hilke, H. Rösner, G. Laplanche, S.V. Divinski, G. Wilde, Tracer diffusion in the σ phase of the CoCrFeMnNi system, Acta Mater. 203 (2021).
[29] R. Li, B. Bian, G. Wilde, Y. Zhang, S.V. Divinski, Bulk and grain boundary tracer diffusion in multiphase AlCoCrFeNi$Ti_{0.2}$ compositionally complex alloy, Acta Mater. 261 (2023), 119352.
[30] M.C. Gao, B. Zhang, S. Guo, J. Qiao, J. Hawk, High-entropy alloys in hexagonal close-packed structure, Metall. Mater. Trans. A 47 (2016) 3322.
[31] R. Soler, A. Evirgen, M. Yao, C. Kirchlechner, F. Stein, M. Feuerbacher, D. Raabe, G. Dehm, Microstructural and mechanical characterization of an equiatomic YGdTbDyHo high entropy alloy with hexagonal close-packed structure, Acta Mater. 156 (2018) 86.
[32] Y. Zhang, T.T. Zuo, Z. Tang, M.C. Gao, K.A. Dahmen, P.K. Liaw, Z.P. Lu, Microstructures and properties of high-entropy alloys, Prog. Mater. Sci. 61 (2014) 1.
[33] L. Rogal, P. Bobrowski, F. Körmann, S. Divinski, F. Stein, B. Grabowski, Computationally-driven engineering of sublattice ordering in a hexagonal AlHfScTiZr high entropy alloy, Sci. Rep. 7 (2017) 1.
[34] X. Zhang, S.V. Divinski, B. Grabowski, Ab initio prediction of vacancy energetics in HCP Al-Hf-Sc-Ti-Zr high entropy alloys and the subsystems, Acta Mater. 227 (2022), 117677.
[35] Rogal L., Czerwinski F., P. Jochym, L. Litynska-Dobrzynska, Microstructure and mechanical properties of the novel Hf_{25} Sc_{25} Ti_{25} Zr_{25} equiatomic alloy with hexagonal solid solutions, Mater. Des. 92 (2016) 8.
[36] S. Uporov, S.K. Estemirova, V. Bykov, D. Zamyatin, R. Ryltsev, A single-phase ScTiZrHf high-entropy alloy with thermally stable hexagonal close-packed structure, Intermetallics 122 (2020), 106802.

[37] P. Klugkist, C. Herzig, Tracer diffusion of titanium in α -iron, Phys. Status Solidi (a) 148 (1995) 413.
[38] R. Catherall, W. Andreazza, M. Breitenfeldt, A. Dorsival, G. Focker, T. Gharsa, T. Giles, J. Grenard, F. Locci, P. Martins, S. Marzari, J. Schipper, A. Shornikov, T. Stora, The ISOLDE facility, J. Phys. G: Nucl. Part. Phys. 44 (2017), 094002.
[39] K. Johnston, J. Schell, J. Correia, M. Deicher, H. Gunnlaugsson, A. Fenta, E. David-Bosne, A. Costa, D.C. Lupascu, The solid state physics programme at ISOLDE: Recent developments and perspectives, J. Phys. G: Nucl. Part. Phys. 44 (2017), 104001.
[40] P.E. Blöchl, Projector augmented-wave method, Phys. Rev. B 50 (1994) 17953.
[41] J.P. Perdew, K. Burke, M. Ernzerhof, Generalized Gradient Approximation Made Simple, Phys. Rev. Lett. 77 (1996) 3865.
[42] G. Kresse, J. Furthmüller, Efficient iterative schemes for ab initio total-energy calculations using a plane-wave basis set, Phys. Rev. B 54 (1996) 11169.
[43] G. Kresse, J. Furthmüller, Efficiency of ab-initio total energy calculations for metals and semiconductors using a plane-wave basis set, Comput. Mater. Sci. 6 (1996) 15.
[44] M. Vaidya, S. Sen, X. Zhang, L. Frommeyer, Ł. Rogal, S. Sankaran, B. Grabowski, G. Wilde, S.V. Divinski, Phenomenon of ultra-fast tracer diffusion of Co in HCP high entropy alloys, Acta Mater. 196 (2020) 220.
[45] A. Paul, T. Laurila, V. Vuorinen, S.V. Divinski, Thermodynamics, Diffusion and the Kirkendall Effect in Solids, Springer, 2014, pp. 1–530, vol. 9783319074.
[46] L. Harrison, Influence of dislocations on diffusion kinetics in solids with particular reference to the alkali halides, Trans. Faraday Soc. 57 (1961) 1191.
[47] A.D.L. Claire, The analysis of grain boundary diffusion measurements, British, J. Appl. Phys. 14 (1963) 351.
[48] Suzuoka Toshiro, Exact solutions of two ideal cases in grain boundary diffusion problem and the application to sectioning method, J. Phys. Soc. Jpn. 19 (1964) 839.
[49] H. Okamoto, T. Massalski, et al., Binary alloy phase diagrams, ASM Int., Mater. Park, OH, USA 12 (1990).
[50] Y. Zhao, Understanding and design of metallic alloys guided by phase-field simulations, npj Comput. Mater. 9 (2023) 94.
[51] X. Zhang, B. Grabowski, T. Hickel, J. Neugebauer, Calculating free energies of point defects from *ab initio*, Comput. Mater. Sci. 148 (2018) 249.
[52] X. Zhang, M. Sluiter, Cluster expansions for thermodynamics and kinetics of multicomponent alloys, J. Phase Equilib. Diffus 37 (2016) 44.
[53] X. Zhang, M.H.F. Sluiter, Kinetically driven ordering in phase separating alloys, Phys. Rev. Mater. 3 (2019), 095601.
[54] B. Beaudry, A. Daane, Sc-Ti system and the allotropy of Sc, Trans. Met. Soc. AIME 224 (1962).
[55] E. Savitskii, G. Burkhanov, Equilibrium diagram of the Scandium-Titanium system, TR: Russ. J. Inorg. Chem. 6 (1961) 1253.
[56] H. Okamoto, Sc-Ti (Scandium-Titanium), J. phase equilibria Diffus. 34 (2013) 158.
[57] V. Danilenko, N.Y. Rusetskaya, O. Semenova, V. Yagodkin, Thermodynamic simulation of the Sc - Ti phase diagram, Powder Metall. Met. Ceram. 38 (1999) 376.
[58] S. Sen, New Avenues for Diffusion Studies in Hexagonal Close Packed High Entropy Alloys, Ph.D. thesis, Institute of Materials Physics, University of Münster, 2023.
[59] R. Perez, F. Dyment, G. Linker, H. Dhers, et al., Zr diffusion in α -Ti measured by RBS and HIRBS, J. Nucl. Mater. 217 (1994) 48.
[60] G. Hood, H. Zou, R. Schultz, E. Bromley, J. Jackman, Diffusion of Ti in α -Zr single crystals, J. Nucl. Mater. 217 (1994) 229.
[61] G. Hood, H. Zou, R. Schultz, N. Matsuura, J. Roy, J. Jackman, Self-and Hf diffusion in α -Zr and in dilute, Fe-free, Zr (Ti) and Zr (Nb) alloys, in: Defect and Diffusion Forum, Trans Tech Publ, 1997, pp. 49–54.
[62] S.-L. Shang, B.-C. Zhou, W.Y. Wang, A.J. Ross, X.L. Liu, Y.-J. Hu, H.-Z. Fang, Y. Wang, Z.-K. Liu, A comprehensive first-principles study of pure elements: vacancy formation and migration energies and self-diffusion coefficients, Acta Mater. 109 (2016) 128.
[63] M. Köppers, C. Herzig, M. Friesel, Y. Mishin, Intrinsic self-diffusion and substitutional Al diffusion in α -Ti, Acta Mater. 45 (1997) 4181.
[64] Q. He, Y. Ye, Y. Yang, The configurational entropy of mixing of metastable random solid solution in complex multicomponent alloys, J. Appl. Phys. 120 (2016), 154902.
[65] M.S. Daw, M. Chandross, Sluggish diffusion in random equimolar FCC alloys, Phys. Rev. Mater. 5 (2021), 043603.
[66] X. Zhang, S.V. Divinski, and B. Grabowski, Ab initio machine-learning unveils strong anharmonicity in non-Arrhenius self-diffusion of tungsten, arXiv preprint arXiv:2311.00633, 2023. 10.48550/arXiv.2311.00633.
[67] A.V. Shapeev, Moment tensor potentials: a class of systematically improvable interatomic potentials, Multiscale Model. Simul. 14 (2016) 1153.
[68] W. Kuang, H. Wang, X. Li, J. Zhang, Q. Zhou, Y. Zhao, Application of the thermodynamic extremal principle to diffusion-controlled phase transformations in Fe-C-X alloys: Modeling and applications, Acta Materialia 159 (2018) 16–30.